Dynamically Preparing Robust Bell States in Su-Schrieffer-Heeger Systems

Jia-Nan Wu, 1 Bingsuo Zou, 2 Guojun Jin, 3,4,* and Yongyou Zhang 1,† ¹Beijing Key Laboratory of Nanophotonics & Ultrafine Optoelectronic Systems, School of Physics, Beijing Institute of Technology, Beijing 100081, China. ²MOE & Guangxi Key Laboratory of Processing for Non-ferrous Metals and Featured Materials,

School of Physical science and Technology, Guangxi University, Nanning 530004, China. ³School of Physics Science and Technology, Kunming University, Kunming 650214, China. ⁴National Laboratory of Solid State Microstructures, Department of Physics, and Collaborative Innovation Center of Advanced Microstructures, Nanjing University, Nanjing 210093, China.

Quantum entanglement is essential for modern quantum information processing. Entanglement gates convert initially non-entangled states into entangled ones by applying time-dependent parametric pulses. While Bell state preparation has been experimentally validated in various platforms, its stability and fidelity are constrained by environmental decoherence and parametric fluctuations. Here, we propose a dynamical framework for preparing robust Bell states by leveraging time-boundary engineering and momentum-space projective measurements within Su-Schrieffer-Heeger (SSH) systems. Employing Lindblad master equation, we theoretically demonstrate that the prepared Bell states exhibit remarkable robustness against both environmental decoherence

(Dated: August 26, 2025)

and parametric time fluctuations, achieving a nearly perfect quantum fidelity, with momentum conservation law governing this robust behavior. To enrich Bell states in momentum space, multi-band SSH models are designed to induce multifold time scattering processes. This time-boundary engineering framework is applicable to both fermionic and bosonic excitations, offering a robust paradigm for generating Bell states in quantum communication and quantum computation.

Quantum entanglement [1], a fundamental signature of quantum mechanics, serves as the cornerstone for quantum information processing [2, 3]. This nonclassical phenomenon enables quantum superdense coding [4], entanglement-based teleportation [5], entanglement swapping [6], quantum key distribution protocols [7], and quantum secret processing [8]. Among various entangled states, two-qubit maximally entangled Bell states [9-13] occupy a privileged position due to their operational simplicity and mathematical elegance. Defined in the Hilbert space $\mathcal{H}_1 \otimes \mathcal{H}_2$ as

$$|\phi^{\pm}\rangle = \frac{1}{\sqrt{2}}(|00\rangle \pm |11\rangle), \quad |\psi^{\pm}\rangle = \frac{1}{\sqrt{2}}(|01\rangle \pm |10\rangle),$$

these states achieve the maximal von Neumann entropy $S(\rho) = -\text{Tr}(\rho \log_2 \rho) = 1$, establishing them as fundamental bases for quantum computation [2] and quantum communica-

The experimental realization of Bell states has been demonstrated across diverse physical platforms, including ion hyperfine states [17], electron spin states [18], photon polarization states [19, 20] or different frequency states [21]. However, two critical challenges persist in practical implementations: (i) Environmental decoherence processes that degrade quantum fidelity through system-bath coupling [13]. (ii) Parametric sensitivity in Hamiltonian engineering. These considerations motivate the development of robust Bell state generation protocols capable of simultaneously suppressing environmental decoherence and compensating parametric time fluctuations.

Compared with conventional spatial modulation systems, such as quantum emitters coupled to waveguides [22] and curved topological boundaries [23], the controlled systems in this work employ time-dependent Hamiltonians to dynamically reconfigure energy band structures without spatial structural modifications [3, 24]. With respect to spacetime modulation in classical optics [26, 27], this approach introduces a novel control freedom for quantum-wave manipulation, namely, time-boundary engineering [28–30], where abrupt time parameter discontinuities modulate quantum dynamics. Upon encountering time boundaries, propagating wave packets undergo velocity bifurcation characterized by time scattering processes, namely, time reflection and time refraction [31–33]. Time reflection exhibits group velocity reversal [34–36], while time refraction maintains group velocity direction [37]. The inherent time-reversal symmetry breaking imposes strict momentum conservation during time scattering processes, resulting in energy redistribution on band branches. This energy-momentum decoupling has been experimentally validated in Su-Schrieffer-Heeger (SSH) momentum lattices [3], demonstrating high scattering efficiency. Other diverse platforms also revealed intriguing phenomena and applications of time-boundary engineering, including photonic time crystals [38, 39] and Floquet metamaterials [40]. This transition from spatial to temporal control paradigms introduces unprecedented capabilities for addressing specific quantum challenges while maintaining robustness against environmental perturbations. Breakthroughs in time-modulated control technologies motivate re-examination of Bell state preparation methodologies.

In quantum information, entanglement gate operations use abrupt or gradual time-dependent parametric pulses to convert initially non-entangled states into entangled ones. Here, we report the preparation of Bell states within a

^{*} gjin@nju.edu.cn

[†] yyzhang@bit.edu.cn

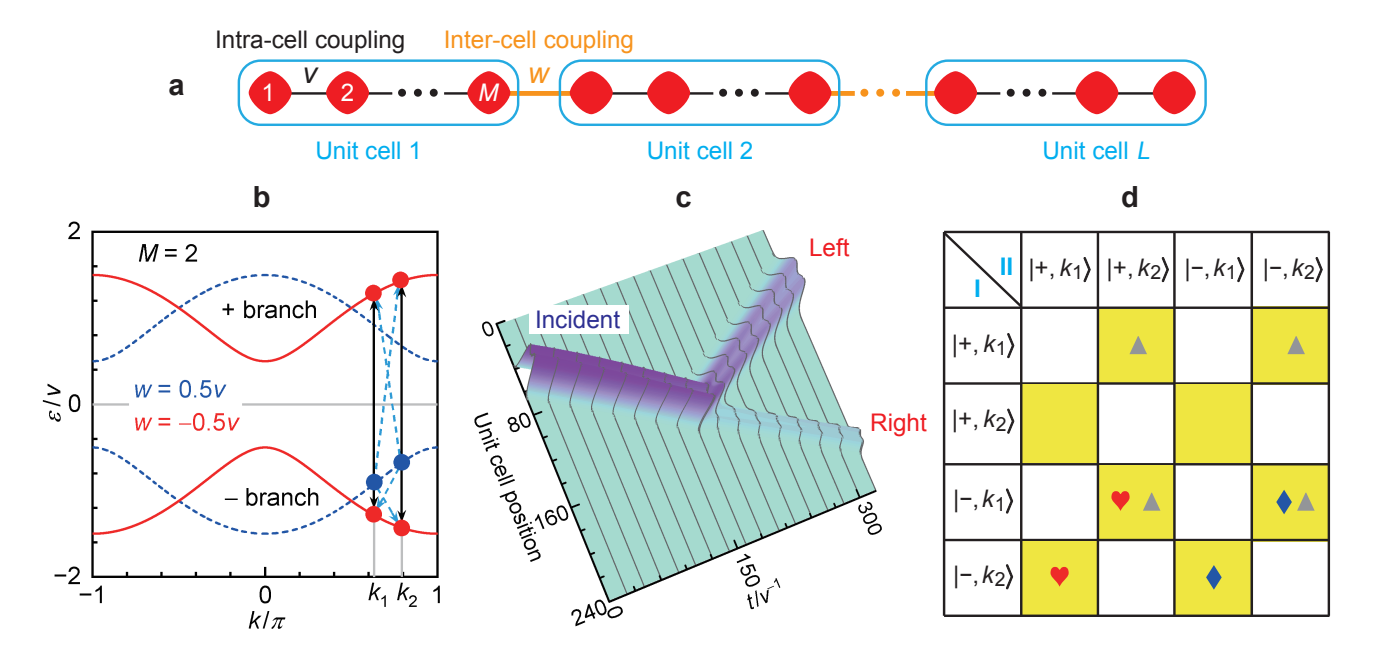


Figure 1. Schematics of time-boundary engineering for decoherence-resistant Bell state generation. **a.** One-dimensional modified SSH model with M sites per unit cell, intra-cell coupling strength v (thin bonds), and inter-cell coupling strength w (thick bonds). The parameter L denotes the total number of unit cells. **b.** Band structures of two SSH models (M=2) with w=0.5v (blue dashed lines, before time boundary t_c) and -0.5v (red solid lines, after t_c). Arrows show the possible two-particle jumping processes across t_c . **c.** Time reflection (left) and refraction (right) phenomena for an incident two-particle Gaussian-type pulse in a fermionic SSH model. Here, the parameters take L=240, M=2, $k_1=0.49\pi$, $k_2=0.51\pi$, and $k_w=0.08\pi$, including w=0.5v and -0.5v before and after the time boundary of $t_c=160v^{-1}$. **d.** Sixteen possible two-particle momentum states arising from the incident state (blue diamonds) with wave vectors k_1 and k_2 . Momentum conservation restricts these to eight yellow-background states. Further, the momentum-distinguishable projection \hat{Q}_B narrows these to four triangle-marked states, while the band-distinguishable projection \hat{Q}_M singles out two heart-marked states.

Su–Schrieffer–Heeger (SSH) model (Fig. 1a, M = 2) using two-particle states scattered by time boundaries, where the SSH lattice is constructed in real-space coordinates [2]. The two involved qubits, $|0\rangle$ and $|1\rangle$, are the excitation states on the two energy bands. The operational entanglement framework is employed to quantify entanglement in indistinguishable two-particle systems [1, 43], involving projection of entangled subspaces from the total Hilbert space, followed by calculations of von Neumann entropies, S. Our work proceeds as follows. Firstly, within plane wave framework, we derive analytical expressions for system parameters required to construct Bell states. Then a dynamical framework based on time-boundary engineering and momentum-space projective measurements is suggested for generating robust Bell states, applicable to both fermionic and bosonic excitations. This framework leads to the projected states in an entanglement-maximum subspace. Subsequent simulations with Gaussian-shaped incident pulses demonstrate that the prepared Bell states exhibit robustness to time boundary variations, environmental decoherence, and parametric perturbations. Note that this robustness roots in momentum conservation law rather than the topological properties inherent from the SSH model [44]. Finally, to enrich Bell states under this framework, the SSH model with M=2 is generalized to an M-band one with M>2 (Fig. 1a). As M > 2, the SSH model is able to support multifold time-scattering processes. The entanglement analysis shows a high-fidelity momentum entanglement between each pair of energy bands. This methodology enables deterministic Bell state preparation through time-boundary engineering, achieving a nearly perfect entanglement fidelity (> 99% even the amplitude of parametric perturbations achieve 4%) that facilitates fault-tolerant quantum implementation.

Results

Time scattering mechanism

The considered SSH model in Fig. 1a consists of L unit cells, each containing M lattice sites, with intra-cell coupling strength v (thin bonds) and inter-cell coupling strength w (thick bonds). The Hamiltonian of this system reads,

$$\hat{\mathcal{H}} = \sum_{l=1}^{L} \sum_{m=1}^{M-1} v \hat{a}_{l,m}^{\dagger} \hat{a}_{l,m+1} + \sum_{l=1}^{L-1} w(t) \hat{a}_{l,M}^{\dagger} \hat{a}_{l+1,1} + \text{h.c.},$$
 (1)

where $\hat{a}^{\dagger}_{l,m}$ ($\hat{a}_{l,m}$) denotes the creation (annihilation) operator for a particle or excitation at the *m*-th site of the *l*-th unit cell. A time boundary would be realized by introducing time dependence into the inter-cell coupling strength, denoted as w(t). The intra-cell coupling strength v is set as energy unit, with its inverse v^{-1} serving as time unit. For notational simplicity, we set the reduced Planck constant $\hbar \equiv 1$ throughout this work.

Starting from the conventional SSH model with M=2, we analyze the time scattering mechanism. The dispersion

relation of the Hamiltonian $\hat{\mathcal{H}}$ is given by

$$\varepsilon_{\pm} = \pm \sqrt{w^2 + v^2 + 2wv\cos k},\tag{2}$$

where the lattice constant is set to unity. The corresponding eigenstates are

$$|\pm, k\rangle \equiv \left[g_{1,k}^{(\pm)}, g_{2,k}^{(\pm)}\right]^T = \frac{1}{\sqrt{2}} \left[1, \pm e^{i\phi_k}\right]^T,$$
 (3)

with the phase factor defined as $e^{i\phi_k} \equiv \frac{1+\eta e^{ik}}{|1+\eta e^{ik}|}$, where $\eta \equiv w/v$ represents the normalized inter-cell coupling strength. The band structure evolves with w, see Fig. 1b for w = 0.5v (blue lines) and w = -0.5v (red lines). An abrupt transition of the inter-cell coupling w from 0.5v to -0.5v induces a splitting of an initial wave into scattered components — an effect termed the time boundary effect. This phenomenon ensures momentum conservation during wave scattering. In Fig. 1b, black solid arrows depict the splitting processes of singleexcitation waves localized at blue dots into scattered waves centered at red dots. For double-excitation waves, additional cross-splitting processes occur, as indicated by blue dashed arrows. The group velocity dictates the propagation direction of scattered waves. For the red bands in Fig. 1b, scattered waves on the upper (ε_+) energy branch propagate to the right, whereas those on the lower (ε_{-}) branch propagate to the left. Figure 1c illustrates a two-excitation incident pulse split into right-propagating and left-propagating components via time scattering.

For the SSH model of M > 2 (or other more general one-dimensional periodical lattice), the time boundary gives rise to additional scattering processes. The theoretical analysis can be straightforwardly extended from the established methodologies for M = 2 SSH model, as detailed in Sec. I of Supplementary material (SM). Notably, the framework applies to both fermionic and bosonic excitations, showcasing its broad applicability across different particle statistics.

Conditions for Bell states

To investigate the parametric regime for constructing Bell states, we consider the SSH model with M=2 and a two-particle plane wave

$$|i\rangle = \hat{a}_{-,k_1}^{\dagger} \hat{a}_{-,k_2}^{\dagger} |0\rangle \tag{4}$$

as the incident state, where $|0\rangle$ denotes the vacuum state with no particle across all lattice sites. The momentum-space creation operator, defined as

$$\hat{a}_{\alpha,k}^{\dagger} = \frac{1}{\sqrt{L}} \sum_{l,m} \hat{a}_{l,m}^{\dagger} g_{m,k}^{(\alpha)} e^{ikl},$$

corresponds to the SSH eigenmode $|\alpha, k\rangle$ ($\alpha = \pm$) before time boundary. Here, $k_1 \neq k_2$ is assumed, a condition valid for both fermionic and bosonic excitations. The initial state $|i\rangle$, marked by two blue diamonds in Fig. 1d, evolves into

$$|f\rangle = \sum_{\alpha\beta,kk'} \psi_{k,k'}^{(\alpha,\beta)} \hat{b}_{\alpha,k}^{\dagger} \hat{b}_{\beta,k'}^{\dagger} |0\rangle, \tag{5}$$

after time scattering. The creation operator $\hat{b}_{\alpha,k}^{\dagger}$ associates with the post-boundary α -branch eigenstate, distinct from the pre-boundary operator $\hat{a}_{\alpha,k}^{\dagger}$. At time boundary, the normalized inter-cell coupling strength η transitions from η_i to η_f . From the incident state $|i\rangle$ with wave vectors k_1 and k_2 , sixteen possible two-particle momentum states emerge in the form $|\alpha,k\rangle|\beta,k'\rangle$, where $\alpha,\beta\in\{+,-\}$ and $k,k'\in\{k_1,k_2\}$ (Fig. 1d). However, momentum conservation restricts these to eight states $|\alpha,k_1\rangle|\beta,k_2\rangle$ and $|\alpha,k_2\rangle|\beta,k_1\rangle$ $(\alpha,\beta\in\{+,-\})$, highlighted by yellow backgrounds. For bosonic and fermionic excitations, their coefficients satisfy $\psi_{k_1,k_2}^{(\alpha,\beta)}=+\psi_{k_2,k_1}^{(\beta,\alpha)}$ and $\psi_{k_1,k_2}^{(\alpha,\beta)}=-\psi_{k_2,k_1}^{(\beta,\alpha)}$, respectively (Sec. II of SM)

For an indistinguishable two-particle state, leveraging the quantum resources encoded in $|f\rangle$ presents a non-trivial challenge. Here, we employ projective measurements to characterize operational entanglement [1]. In the context of $|f\rangle$, two possible approaches exist for defining projective measurement operators. The first utilizes momenta to distinguish excitations, designating those with k_1 and k_2 as particles I and II, respectively. The corresponding projection operator is $Q_B = \sum_{\alpha,\beta \in \{+,-\}} |\alpha\rangle_I |\beta\rangle_{II II} \langle\beta|_I \langle\alpha|$, where $|\alpha\rangle_I \equiv |\alpha,k_1\rangle$ and $|\beta\rangle_{\rm II} \equiv |\beta, k_2\rangle$. $\hat{Q}_{\rm B}$ measures the branch-correlation between particles I and II, encompassing four states highlighted by gray triangles in Fig. 1d. These states indicate that the postmeasurement density operator $\hat{\rho}=\hat{Q}_{\rm B}|f\rangle\langle f|\hat{Q}_{\rm B}^{\dagger}$ does not guarantee high entanglement (Sec. II of SM). Experimentally, distinguishing particles by momenta further complicates this approach.

The alternative approach involves distinguishing excitations by their band branches, assigning those on the – and + branches as particles I and II, respectively. The associated projection operator is

$$\hat{Q}_{\mathrm{M}} = \sum_{k,k' \in \{k_{1},k_{2}\}} |k\rangle_{\mathrm{II}} |k'\rangle_{\mathrm{II}} |\mathbf{II}\langle k'| |\mathbf{I}\langle k|,$$
 (6)

where $|k\rangle_{\rm I} \equiv |-,k\rangle$ and $|k'\rangle_{\rm II} \equiv |+,k'\rangle$. Momentum conservation restricts $\hat{Q}_{\rm M}$ to two states $|k_1\rangle_{\rm I}|k_2\rangle_{\rm II}$ and $|k_2\rangle_{\rm I}|k_1\rangle_{\rm II}$, marked by two red hearts in Fig. 1d. Owing to distinct group velocities of particles I and II, $\hat{Q}_{\rm M}$ exhibits at least two key advantages: (i) Spatial separability of particles I and II, see Fig. 1c; (ii) The post-measurement density operator $\hat{\rho}_{\rm M} = \hat{Q}_{\rm M}|f\rangle\langle f|\hat{Q}_{\rm M}^{\dagger}$ can characterize a Bell state in momentum space. To determine the condition, we express the projection of $|f\rangle$ via $\hat{Q}_{\rm M}$ as

$$|f_Q\rangle = \hat{Q}_{\mathrm{M}}|f\rangle = \psi_{k_1,k_2}|k_1\rangle_{\mathrm{I}}|k_2\rangle_{\mathrm{II}} + \psi_{k_2,k_1}|k_2\rangle_{\mathrm{I}}|k_1\rangle_{\mathrm{II}}.$$
 (7)

The condition $|\psi_{k_1,k_2}| = |\psi_{k_2,k_1}|$ renders $|f_Q\rangle$ a Bell state in momentum space. Setting $k_1 = k_0 - \Delta k/2$ and $k_2 = k_0 + \Delta k/2$, the parametric equation

$$\cos k_0 = -\frac{\eta_i + \eta_f}{1 + \eta_i \eta_f} \quad (\eta_i \neq \eta_f; \ \eta_i, \eta_f \notin \{0, 1\})$$
 (8)

ensures $\psi_{k_1,k_2} = +\psi_{k_2,k_1}$ for bosonic excitations while $\psi_{k_1,k_2} = -\psi_{k_2,k_1}$ for fermic excitations, up to leading order in $O(\Delta k)$. The regime of the solutions of Eq. (S16), see Fig. 2a, satisfies

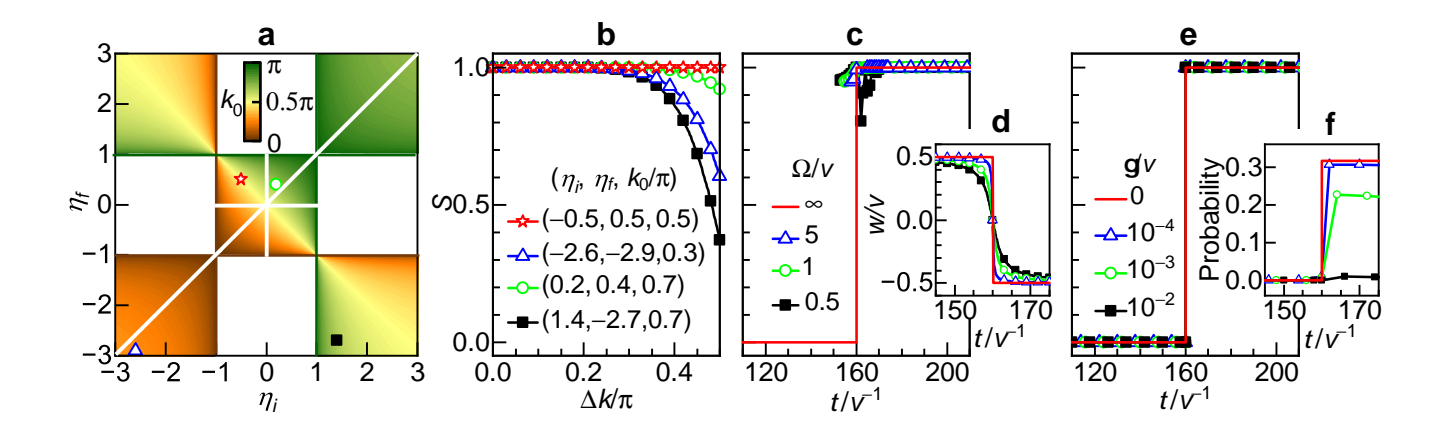


Figure 2. Parametric dependence for Bell state construction. **a.** Parameter regime for achieving Bell states, valid for both fermionic and bosonic models. **b.** Variations of the von Neumann entropy S of $|f_Q\rangle$ with the wave vector difference Δk of two excitations at the four characteristic points marked in **a. c.** Time evolution of S under four types of time boundaries, illustrating the robustness of entanglement against boundary gradual change. **d.** Corresponding w(t) profiles for the time boundaries used in **c. e.** Time evolution of S under four different decoherence rates γ , assessing the entanglement robustness of Bell states to environmental decoherence. **f.** Bell state probabilities corresponding to **e.** Parameters: In **a** and **b**, step time boundaries are applied with no decoherence; in **c-f**, $k_0 = 0.5\pi$, $\Delta k = 0.02\pi$, $k_w = 0.08\pi$, and $t_c = 160v^{-1}$; **c** and **d** assume no decoherence, while **e** and **f** account for decoherence and incorporate step time boundaries; in **b-f**, the fermionic SSH model (M = 2) is used.

either $|\eta_i|<1$ and $|\eta_f|<1$, or $|\eta_i|>1$ and $|\eta_f|>1$. In particular, when

$$\eta_i + \eta_f = 0, \quad k_0 = \frac{\pi}{2},$$
(9)

the relation $\psi_{k_1,k_2} \equiv \pm \psi_{k_2,k_1}$ holds for any Δk , implying that $|f_Q\rangle$ can be engineered as a Bell state (see the proof in Sec. II of SM).

Figure 2a illustrates the parametric regime defined by Eq. (S16) for Bell state construction, with four points selected to plot the von Neumann entropy of $|f_O\rangle$,

$$S = -|\psi_{k_1,k_2}|^2 \log_2 |\psi_{k_1,k_2}|^2 - |\psi_{k_2,k_1}|^2 \log_2 |\psi_{k_2,k_1}|^2,$$

as a function of Δk in Fig. 2b. When $\eta_i = -\eta_f$ and $k_0 = \frac{\pi}{2}$, the entropy strictly equals 1 (see point star in Fig. 2a and red stardotted line in Fig. 2b), signifying maximal entanglement. For the remaining three solutions, the entropies show a decline as Δk surpasses 0.2π . Notably, when $\Delta k < 0.2\pi$, the state $|f_Q\rangle$ remains close to the maximum entanglement limit. The parametric regime is sufficiently broad to facilitate Bell state construction.

In additional to the time boundary introduced by tuning η , the temporal tuning of onsite energies can also give rise to Bell states with better performance, see Sec. III of SM.

Gradual time boundary

The above discussions and results are based on the planewave initial state as Eq. (S48) under a step time boundary. This section utilizes a more general Gaussian wavefunction as

$$|i_{G}\rangle = \sum_{l_{1},m_{1},l_{2},m_{2}} \psi_{l_{1},m_{1}} \psi_{l_{2},m_{2}} \hat{a}_{l_{1},m_{1}}^{\dagger} \hat{a}_{l_{2},m_{2}}^{\dagger} |0\rangle, \tag{10}$$

to explore the impact of a gradual time boundary. The wave amplitude is defined as

$$\psi_{l_n,m_n} \propto \sum_k e^{-\frac{(k-k_n)^2}{k_w^2}} g_{m_n,k}^{(-)} e^{ik(l_n-x_{0,n})},$$

characterized by a wave vector width k_w , two wave vector centers k_n , and two initial position centers $x_{0,n}$. Without loss of generality, we take the fermionic SSH model as examples in the following numerical simulations.

The time-dependent Schrödinger equation dictates the evolution of the state $|i_G\rangle$. After the gradual time scattering, it enables us to calculate the von Neumann entropy S between the two particles in the projective state $|f_Q\rangle$. The gradual time boundary around t_c is mathematically described by

$$w(t)/v = -\frac{1}{\pi} \arctan \left[\Omega(t - t_c)\right],$$

where, as the parameter Ω increases from 0 to ∞ , the boundary smoothly transforms into a step boundary (Fig. 2d). Notably, the state $|f_Q\rangle$ remains a pure state regardless of the type of time boundary considered.

The parametric conditions $\eta_i + \eta_f = 0$ and $k_0 = \frac{\pi}{2}$ guarantee that the entanglement of the state $|f_Q\rangle$ approaches its maximum value, independent of the boundary type, see Fig. 2c. This property is of crucial significance for experimental realizations. Although a slowly-varying time boundary has the potential to disrupt time reflection and refraction phenomena [3], the constructed Bell states exhibit remarkable robustness against the gradual behavior of the time boundary (see the proof in Sec. IV of SM).

Environmental decoherence

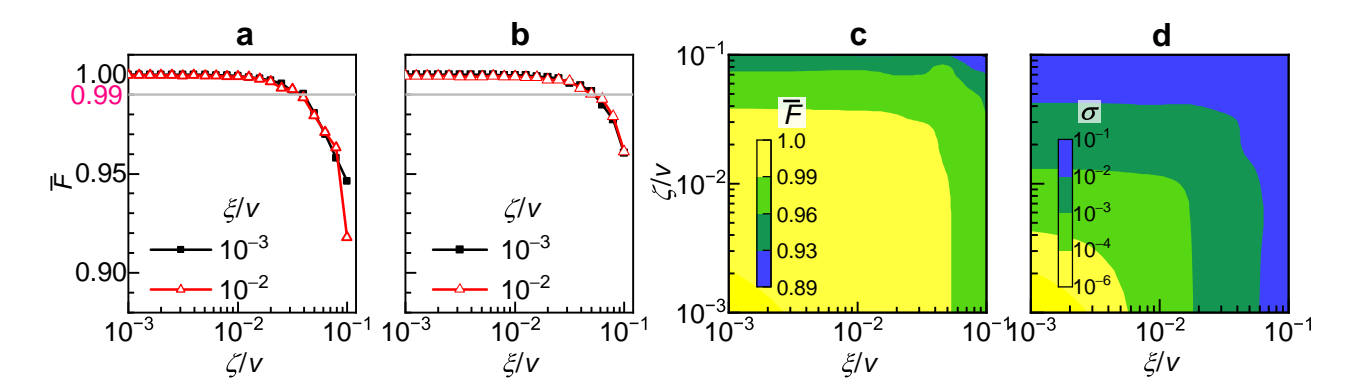


Figure 3. Quantum fidelity of Bell states under parametric time fluctuations. **a.** Mean fidelity \bar{F} of $|f_Q\rangle_{\rm Rand}$ at $t=320v^{-1}$, varying with ζ under different values of ξ . **b.** \bar{F} of $|f_Q\rangle_{\rm Rand}$ at $t=320v^{-1}$, varying with ξ under different values of ζ . **c** and **d**. Contour maps of mean fidelity \bar{F} and standard deviation σ in the ζ - ξ parameter space for $|f_Q\rangle_{\rm Rand}$ at $t=320v^{-1}$. Parameters: $\eta_i=-\eta_f=0.5, k_0=0.5\pi, \Delta k=0.02\pi, k_w=0.08\pi,$ and $t_c=160v^{-1}$; in **a-d**, the fermionic SSH model (M=2) is used.

Environmental decoherence presents another critical challenge to the realization of reliable quantum processing. Useful techniques to mitigate decoherence induced effects include quantum information masking [45], quantum error correction [46], dynamical decoupling [47], and adopting decoherence-free subspaces [46–48]. Identifiably, the quantum states constructed in this work reside in an entanglement-maximum subspace, rendering them insensitive to environmental decoherence. To demonstrate this, we utilize the Lindblad master equation,

$$\frac{d\hat{\rho}}{dt} = -i\left[\hat{\mathcal{H}}, \ \hat{\rho}\right] + \gamma \sum_{l,m} \left(\hat{a}_{l,m}\hat{\rho}\hat{a}_{l,m}^{\dagger} - \frac{1}{2}\left\{\hat{\rho}, \hat{a}_{l,m}^{\dagger}\hat{a}_{l,m}\right\}\right),\,$$

where γ quantifies the decoherence rate acting on the density operator $\hat{\rho}$. The master equation is solved through fourth-order Runge-Kutta method iteratively and the initial density operator is defined as $\hat{\rho}_0 = |i_G\rangle\langle i_G|$ via Eq. (10). Following time evolution, the post-measurement density operator

$$\hat{\rho}_{\rm M} = \hat{Q}_{\rm M} \hat{\rho} \hat{Q}_{\rm M}^{\dagger}$$

remains pure, even as $\hat{\rho}$ becomes mixed due to decoherence $(\gamma > 0)$. The von Neumann entropy, $S = -\text{Tr}(\tilde{\rho}_M \log_2 \tilde{\rho}_M)$ with $\tilde{\rho}_M \propto \text{Tr}_{II}(\hat{\rho}_M)$, is employed to quantify momentum entanglement, as illustrated in Fig. 2e under a step time boundary condition. Notably, $\hat{\rho}_M$ consistently attains the maximum entanglement limit, irrespective of the decoherence rate (see the proof in Sec. V of SM).

However, decoherence substantially affects the success probability (measured by $\text{Tr}(\hat{\rho}_{\text{M}})$) of Bell state generation. Figure 2f demonstrates that this probability drops from 31.6% to ~20% and then to ~1% as γ increases from 0 to 0.001 ν and then to 0.01 ν . This behavior is physically intuitive, as decoherence rate γ reduces the number of excitations within the system. The pivotal insight is that while decoherence diminishes the success probability, it exerts a surprisingly weak influence on the entanglement of the constructed states. The constructed states exist within an entanglement-maximum subspace, effectively safeguarded from the impacts

of decoherence.

Parametric fluctuation

Experimental systems inherently suffer from parametric time fluctuations that may affect eigenstates and band structures during time evolution. Thus, it is critical to assess how such perturbations impact the prepared Bell states. We focus on two types of perturbations: hopping parameters v and w, and onsite energies. Note that onsite energies are set to zero in the Hamiltonian of Eq. (1). Without loss of generality, the perturbation amplitudes for v and w are assumed identical, denoted by ζ , and that for onsite energies denoted by ξ . White noise perturbations are modeled as $v \to v + \zeta \cdot \text{Rand}(t)$, where Rand(t) is a random number in (-1, 1). Using the Gaussiantype initial state of Eq. (10) and the projection operator \hat{Q}_{M} , we characterize the final state $|f_Q\rangle_{\text{Rand}}$ under parametric perturbations.

The quantum fidelity of $|f_O\rangle_{Rand}$ is defined as

$$F = \left| \langle f_Q | f_Q \rangle_{\text{Rand}} \right|^2,$$

where $|f_Q\rangle$ corresponds to the unperturbed state ($\zeta = \xi = 0$). Figures ${\bf 3a}$ and ${\bf 3b}$ illustrate the variations of the statistical mean quantum fidelity $\bar F$ with respect to ζ and ξ , respectively. In calculations, the parameters $k_0 = 0.5\pi$ and $\eta_i = -\eta_f = 0.5$, according to Eq. (9), are adopted to ensure $|f_Q\rangle$ represents a Bell state. $\bar F$ is obtained via statistical averaging over 100 disordered time evolution processes. As expected, large parametric fluctuations substantially degrade the fidelity. However, when ζ and ξ are below $\sim 0.04\nu$, $\bar F$ remains above 0.99, indicating that $|f_Q\rangle_{\rm Rand}$ closely approximates the ideal Bell state.

Figure 3c presents a contour map of \bar{F} in the ζ - ξ space. The yellow region ($\bar{F} > 0.99$) confirms the robustness of $|f_Q\rangle_{\rm Rand}$ against parametric time perturbations. Correspondingly, the standard deviation σ of F, shown in Fig. 3d, is less than 0.01, further validating the stability of the scheme. Relaxing the fidelity threshold to $\bar{F} > 0.9$ allows parametric fluctuations up to $\sim 0.1v$ (Figs. 3a-3c). Accordingly, the dynamical framework based on time-boundary engineering has a strong

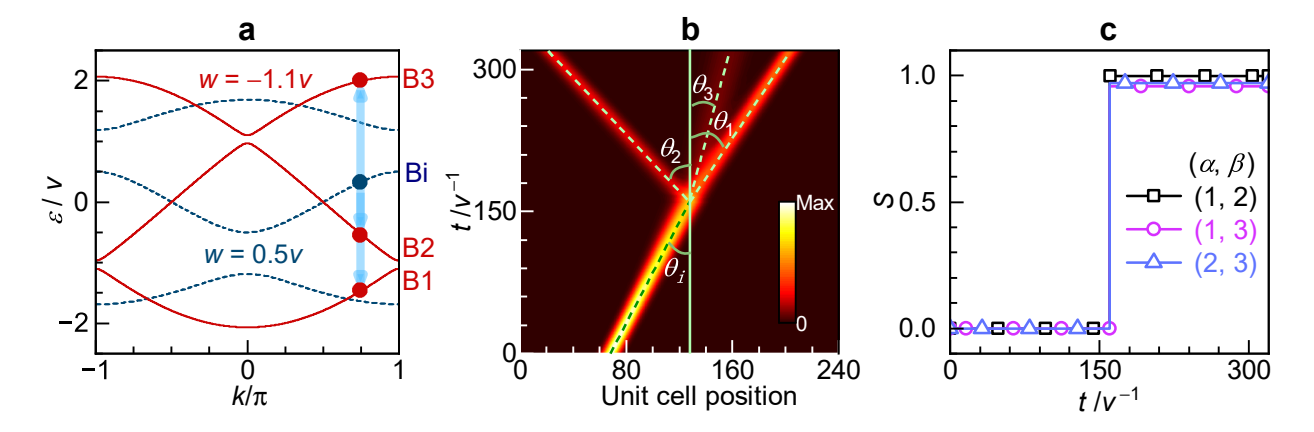


Figure 4. High-entangled states induced by multifold time scattering. **a.** The band structures of the three-band system (M=3 in Fig. 1a) with w=0.5v (before time boundary) and w=-1.1v (after time boundary). **b.** Schematic of the three-fold time scattering. **c.** Time evolution of S for the projected states that two particles distribute on different bands. Parameters: $k_0=0.75\pi$, $\Delta k=0.02\pi$ $k_w=0.08\pi$, $x_0=69$, $\eta_i=0.5$, $\eta_f=-1.1$, $t_c=160v^{-1}$; in **a-c**, the fermionic SSH model (M=3) is used.

robustness against parametric time fluctuations.

Multifold time scattering

The preceding discussions have illustrated the momentum entanglements of two particles on the two energy bands within the SSH model. To enrich such entanglement states, the conventional SSH model is extended into a multi-band framework by setting M > 2 (Fig. 1a). As an instance, when M = 3, the band structures for w = 0.5v (dashed lines) and w = -1.1v (solid lines) are depicted in Fig. 4a. This multi-band system enables multifold time scattering processes, significantly enriching entanglement states in momentum space.

Similar to the M = 2 case, when w undergoes an abrupt transition from 0.5v to -1.1v, a step time boundary can be introduced to manipulate the state distribution. The initial state $|i\rangle$ is localized around the dark-blue dot on the initial band 'Bi'. Due to the time boundary, this state is scattered into three energy bands (B1, B2, and B3), where momentum conservation leads to the final states primarily accumulating around the three red dots in Fig. 4a. Notably, the group velocities of the three bands near these red dots exhibit distinct values in momentum space. This difference in group velocities gives rise to multifold time scattering. As illustrated in Fig. 4b, a Gaussian-type initial single-excitation state with a wave vector center at $k_0 = 0.75\pi$ and width $k_w = 0.08\pi$ is utilized. Here, θ_i denotes the incident angle relative to the time boundary. Specifically, θ_1 , θ_2 , and θ_3 represent the scattering angles corresponding to bands B1, B2, and B3, respectively. These angles are determined by the group velocities of the eigenstates in each band (Sec. VI of SM), analogous to the time reflection and refraction phenomena in the M=2 case.

Bell states in momentum space can be constructed on any pair of energy bands in the multi-band system. Taking an initial two-excitation Gaussian state like Eq. (10) on the 'Bi' band as an example, the parameters are set as $k_0 = 0.75\pi$, $\Delta k = 0.02\pi$, $\eta_i = 0.5$, and $\eta_f = -1.1$. The projective operator $\hat{Q}_{\rm M}$ is extended to $\hat{Q}_{\rm M}^{(\alpha,\beta)}$ to accommodate three energy bands

(B1, B2, B3),

$$\hat{Q}_{\rm M}^{(\alpha,\beta)} = \sum_{k,k'} |\alpha,k\rangle_{\rm I} |\beta,k'\rangle_{\rm II\ II} \langle \beta,k'|_{\rm I} \langle \alpha,k|, \tag{11}$$

where $\alpha, \beta \in \{1, 2, 3\}$. After time scattering, the von Neumann entropies S for the projected states via $\hat{Q}_{\rm M}^{(1,2)}$, $\hat{Q}_{\rm M}^{(1,3)}$, and $\hat{Q}_{\rm M}^{(2,3)}$ are shown in Fig. 4c, indicating high entanglement under specific parametric conditions (see Sec. VI of SM). Compared to the conventional SSH model, the multi-band system significantly enriches entanglement states. The total number of $\{\alpha, \beta\}$ combinations increases with band number M as M(M-1)/2, highlighting the scalability of entanglement resources.

Conclusion and outlook

In this work, we introduce time boundaries into the SSH model and utilize projective measurements to prepare twoparticle Bell states in momentum space. We derive the parametric conditions for these Bell states and confirm their remarkable robustness against momentum difference between the two particles, gradual time boundaries, and environmental decoherence. Such a robustness dates from momentum conservation law. The prepared Bell states maintain high fidelity even under significant parametric time fluctuations. Specifically, the fidelity of the prepared Bell states exceeds 99% even as the stochastic disturbances of onsite energies or site-site coupling strengths reach 4%. By generalizing the SSH model to a multi-band system through adding additional sites per unit cell, we induce multifold time scattering. This process also gives rise to high momentum entanglements between two particles on each pair of energy bands, which enriches entanglement resources. Our study establishes a dynamical framework for the preparation of the high-fidelity Bell states, applicable to both fermionic and bosonic excitations, thereby advancing potential applications in quantum technologies.

Furthermore, topologically protected edge states in twodimensional (2D) lattices—characterized by robustness against local perturbations [23]—have been extensively investigated. Concurrently, the interplay between band topology and temporal boundary effects has been established [29]. These foundational studies indicate that the dynamical framework for preparing robust Bell states, which relies on time-boundary engineering and momentum-space projective measurements, could also achieve topological robustness against local stochastic disturbances when implemented in topological systems.

Method

Operational entanglement

Generally, an indistinguishable two-body state does not inherently contain quantum entanglement [1]. To extract entanglement from such a system, it is necessary to project the entangled component by assigning specific indices to each particle within the total state. For example, consider a two-particle state $|f\rangle = \sum_{\{k_1k_2\}} \zeta_{k_1k_2} |k_1, k_2\rangle$ in momentum (k) space.

The projective operator $\hat{Q}_{ab} = \sum_{k_1k_2} |k_1\rangle_a |k_2\rangle_b \, _b \langle k_2| \, _a \langle k_1|$ is defined to label the two subspaces with indices a and b. Applying this operator yields the projected entangled state $|f_{ab}\rangle = \hat{Q}_{ab}|f\rangle = \sum_{k_1k_2} \xi_{k_1k_2} |k_1\rangle_a |k_2\rangle_b$, where $\sum_{k_1k_2} |\xi_{k_1k_2}|^2$ represents the probability of the entangled state. The density matrix of $|f_{ab}\rangle$ is $\rho_{ab} = |f_{ab}\rangle\langle f_{ab}|$, and the reduced density matrix for subsystem a is $\rho_a = \sum_{k_2} b \langle k_2|\rho_{ab}|k_2\rangle_b$. Using ρ_a , the von Neumann entropy $S = -\text{Tr}(\rho_a \log_2 \rho_a)$ can be obtained to quantify the operational entanglement between the two particles in subspaces a and b. This method provides a rigorous framework for identifying and measuring the entanglement in an indistinguishable two-body system by leveraging index-based projection and entropy-based quantification.

Acknowledgement

This work was supported by the National Natural Science Foundation of China (Grant Nos. 12074037 and 12074156).

- [1] R. Horodecki, P. Horodecki, M. Horodecki, and K. Horodecki, Quantum entanglement, Rev. Mod. Phys. 81, 865 (2009).
- [2] H. Zhang, G.-P. Guo, T. Tu, and G.-C. Guo, Quantum computation and bell-state measurements with double-dot molecules, Phys. Rev. A 76, 012335 (2007).
- [3] S. Slussarenko and G. J. Pryde, Photonic quantum information processing: A concise review, Appl. Phys. Rev. 6, 041303 (2019).
- [4] X. S. Liu, G. L. Long, D. M. Tong, and F. Li, General scheme for superdense coding between multiparties, Phys. Rev. A 65, 022304 (2002).
- [5] S. Pirandola, J. Eisert, C. Weedbrook, A. Furusawa, and S. L. Braunstein, Advances in quantum teleportation, Nat. Photonics 9, 641 (2015).
- [6] S. Liu, Y. Lou, Y. Chen, and J. Jing, All-optical entanglement swapping, Phys. Rev. Lett. 128, 060503 (2022).
- [7] T. Sasaki, Y. Yamamoto, and M. Koashi, Practical quantum key distribution protocol without monitoring signal disturbance, Nature 509, 475 (2014).
- [8] W. Zhang, D.-S. Ding, Y.-B. Sheng, L. Zhou, B.-S. Shi, and G.-C. Guo, Quantum secure direct communication with quantum memory, Phys. Rev. Lett. 118, 220501 (2017).
- [9] N. Gisin and H. Bechmann-Pasquinucci, Bell inequality, bell states and maximally entangled states for n qubits, Phys. Lett. A 246, 1 (1998).
- [10] Y.-H. Kim, S. P. Kulik, and Y. Shih, Quantum teleportation of a polarization state with a complete bell state measurement, Phys. Rev. Lett. 86, 1370 (2001).
- [11] S. Ghosh, G. Kar, A. Roy, A. Sen(De), and U. Sen, Distinguishability of bell states, Phys. Rev. Lett. 87, 277902 (2001).
- [12] Y. Ji, Y. Liu, H. Li, X. Zhou, R. Xiao, L. Dong, and X.-M. Xiu, Fast preparation of bell state and w state with rydberg superatom, Quantum Inf. Process. 19, 1 (2020).
- [13] P. Zhao, Z. Jin, and D. Tong, Dissipative preparation of generalized bell states with the sørensen-mølmer setting, Phys. Rev. Appl. 18, 014051 (2022).
- [14] N. Gisin and R. Thew, Quantum communication, Nat. Photonics 1, 165 (2007).
- [15] Y.-B. Sheng, F.-G. Deng, and G. L. Long, Complete hyperentangled-bell-state analysis for quantum communication,

- Phys. Rev. A 82, 032318 (2010).
- [16] L. Dong, X.-M. Xiu, Y.-J. Gao, Y.-P. Ren, and H.-W. Liu, Controlled three-party communication using ghz-like state and imperfect bell-state measurement, Opt. Commun. 284, 905 (2011).
- [17] C. R. Clark, H. N. Tinkey, B. C. Sawyer, A. M. Meier, K. A. Burkhardt, C. M. Seck, C. M. Shappert, N. D. Guise, C. E. Volin, S. D. Fallek, H. T. Hayden, W. G. Rellergert, and K. R. Brown, High-fidelity bell-state preparation with ⁴⁰ca⁺ optical qubits, Phys. Rev. Lett. 127, 130505 (2021).
- [18] J. Zou, S. Zhang, and Y. Tserkovnyak, Bell-state generation for spin qubits via dissipative coupling, Phys. Rev. B 106, L180406 (2022).
- [19] Y.-S. Kim, T. Pramanik, Y.-W. Cho, M. Yang, S.-W. Han, S.-Y. Lee, M.-S. Kang, and S. Moon, Informationally symmetrical bell state preparation and measurement, Opt. Express 26, 29539 (2018).
- [20] Q.-Y. Wu, Z. Meng, X.-X. Chen, J. Li, J.-Z. Yang, and A.-N. Zhang, Experimental realization of a quantum classification: Bell state measurement via machine learning, APL Mach. Learn. 1 (2023).
- [21] V. Macrì, F. Nori, and A. F. Kockum, Simple preparation of bell and greenberger-horne-zeilinger states using ultrastrongcoupling circuit qed, Phys. Rev. A 98, 062327 (2018).
- [22] J.-T. Shen and S. Fan, Theory of single-photon transport in a single-mode waveguide. i. coupling to a cavity containing a twolevel atom, Phys. Rev. A 79, 023837 (2009).
- [23] J. Dong, B. Zou, and Y. Zhang, Reconfigurable valley topological qed platform for qubit operation, Phys. Rev. A 108, 023513 (2023).
- [24] J. Struckmeier and C. Riedel, Invariants for time-dependent hamiltonian systems, Phys. Rev. E 64, 026503 (2001).
- [3] Z. Dong, H. Li, T. Wan, Q. Liang, Z. Yang, and B. Yan, Quantum time reflection and refraction of ultracold atoms, Nat. Photon. 18, 68 (2024).
- [26] S. Akhmanov, A. Sukhorukov, and A. Chirkin, Nonstationary phenomena and space-time analogy in nonlinear optics, Sov. Phys. JETP 28, 748 (1969).
- [27] B. Kolner, Space-time duality and the theory of temporal imaging, IEEE J. Quantum Electron 30, 1951 (1994).
- [28] Y. Zhou, M. Z. Alam, M. Karimi, J. Upham, O. Reshef, C. Liu,

- A. E. Willner, and R. W. Boyd, Broadband frequency translation through time refraction in an epsilon-near-zero material, Nat. commun. 11, 2180 (2020).
- [29] H. C. Wu, H. S. Xu, L. C. Xie, and L. Jin, Edge state, band topology, and time boundary effect in the fine-grained categorization of chern insulators, Phys. Rev. Lett. 132, 083801 (2024).
- [30] H. Xu, Z. Dong, L. Yuan, and L. Jin, Probing bulk band topology from time boundary effect in synthetic dimension, Phys. Rev. Lett. 134, 163801 (2025).
- [31] J. T. Mendonça and P. K. Shukla, Time refraction and time reflection: Two basic concepts, Phys. Scr. 65, 160 (2002).
- [32] O. Y. Long, K. Wang, A. Dutt, and S. Fan, Time reflection and refraction in synthetic frequency dimension, Phys. Rev. Res. 5, L012046 (2023).
- [33] L. Bar-Hillel, A. Dikopoltsev, A. Kam, Y. Sharabi, O. Segal, E. Lustig, and M. Segev, Time refraction and time reflection above critical angle for total internal reflection, Phys. Rev. Lett. 132, 263802 (2024).
- [34] V. Bacot, M. Labousse, A. Eddi, M. Fink, and E. Fort, Time reversal and holography with spacetime transformations, Nat. Physics 12, 972 (2016).
- [35] H. Moussa, G. Xu, S. Yin, E. Galiffi, Y. Radi, and A. Alú, Observation of temporal reflection and broadband frequency translation at photonic time interfaces, Nat. Physics 19, 863 (2023).
- [36] G. P. Agrawal, Temporal reflection from ultrashort solitons in nonlinear dispersive medium: Impact of raman scattering, in Photonics, Vol. 11 (MDPI, 2024) p. 1189.
- [37] J. T. Mendonça, Time refraction and spacetime optics, Symmetry 16, 1548 (2024).
- [38] Y. Sharabi, A. Dikopoltsev, E. Lustig, Y. Lumer, and M. Segev, Spatiotemporal photonic crystals, Optica 9, 585 (2022).
- [39] Y. Peng, Topological space-time crystal, Phys. Rev. Lett. 128, 186802 (2022).
- [40] C. Weitenberg and J. Simonet, Tailoring quantum gases by floquet engineering. Nat. Phys. 17, 1342 (2021).
- [2] M. Atala, M. Aidelsburger, J. T. Barreiro, D. Abanin, T. Kita-gawa, E. Demler, and I. Bloch, Direct measurement of the zak phase in topological bloch bands, Nature Phys. 9, 795 (2013).
- R. Lo Franco and G. Compagno, Indistinguishability of elementary systems as a resource for quantum information processing, Phys. Rev. Lett. 120, 240403 (2018).
- [43] K. Monkman and J. Sirker, Operational entanglement of symmetry-protected topological edge states, Phys. Rev. Res. 2, 043191 (2020).
- [44] S. Liu, W. Gao, Q. Zhang, S. Ma, L. Zhang, C. Liu, Y. J. Xiang, T. J. Cui, and S. Zhang, Topologically protected edge state in two-dimensional su-schrieffer-heeger circuit, Research 2019 (2019).
- [45] Z.-H. Liu, X.-B. Liang, K. Sun, Q. Li, Y. Meng, M. Yang, B. Li, J.-L. Chen, J.-S. Xu, C.-F. Li, and G.-C. Guo, Photonic implementation of quantum information masking, Phys. Rev. Lett. 126, 170505 (2021).
- [46] N. R. Dash, S. Dutta, R. Srikanth, and S. Banerjee, Concatenating quantum error-correcting codes with decoherence-free subspaces and vice versa, Phys. Rev. A 109, 062411 (2024).
- [47] D. A. Lidar, Review of decoherence-free subspaces, noiseless subsystems, and dynamical decoupling, Quantum information and computation for chemistry, 295 (2014).
- [48] O. Rubies-Bigorda, S. J. Masson, S. F. Yelin, and A. Asenjo-Garcia, Deterministic generation of photonic entangled states using decoherence-free subspaces, Phys. Rev. Lett. 134, 213603 (2025).

SUPPLEMENTARY INFORMATION FOR "DYNAMICALLY PREPARING ROBUST BELL STATES IN SU-SCHRIEFFER-HEEGER SYSTEMS"

Appendix I: Time scattering mechanism for arbitrary M

In this section, we elaborate on the scattering mechanism for waves within the SSH model with arbitrary M. Employing the Hamiltonian given as Eq. (1) of Main text (MT), we begin from the energy eigenvalue equation

$$\hat{\mathcal{H}}|\psi_{\alpha}(k)\rangle = \varepsilon_{\alpha}(k)|\psi_{\alpha}(k)\rangle,\tag{S1}$$

which can be solved by the Bloch-like ansatz

$$|\psi_{\alpha}(k)\rangle = |k\rangle \otimes |u_{\alpha}(k)\rangle = \frac{1}{\sqrt{L}} \sum_{l=1}^{L} e^{ikl} |l\rangle \otimes \sum_{m=1}^{M} g_{m,k}^{(\alpha)} |m\rangle, \tag{S2}$$

with $|l, m\rangle = \hat{a}_{l,m}^{\dagger}|0\rangle$. Instituting Eq. (S2) into (S1) leads to

$$\varepsilon_{\alpha}(k)\mathbf{u}_{\alpha}(k) = \hat{\mathbf{H}}(k)\mathbf{u}_{\alpha}(k). \tag{S3}$$

Taking M = 3 as an example, $\hat{\mathbf{H}}(k)$ and $\mathbf{u}_{\alpha}(k)$ have forms

$$\hat{\mathbf{H}}(k) = \begin{pmatrix} 0 & v & we^{-ik} \\ v & 0 & v \\ we^{ik} & v & 0 \end{pmatrix}, \quad \mathbf{u}_{\alpha}(k) = \begin{pmatrix} g_{1,k}^{(\alpha)} \\ g_{2,k}^{(\alpha)} \\ g_{3,k}^{(\alpha)} \end{pmatrix}. \tag{S4}$$

Through solving Eq. (S3), the eigenvectors $\mathbf{u}_{\alpha}(k)$, dispersion relationship $\varepsilon_{\alpha}(k)$ and thus group velocities $v_{\alpha} = d\varepsilon_{\alpha}(k)/dk$ for arbitrary M can be obtained. In general, the group velocities of different bands are distinct, causing waves on separate bands to spatially disperse as they propagate, which results in an M-fold time scattering.

Appendix II: Parametric conditions for constructing Bell states

This section derives the parametric conditions for constructing Bell states presented in Eq. (8) of the MT. In the MT, we start from the initial state given by Eq. (4), which represents a two-particle plane wave with both particles residing in the lower band. When encountering the time boundary (the system parameter η_i abruptly switches to η_f), the eigenstates of the system transform from

$$\left[g_{1,k}^{(-)}, g_{2,k}^{(-)}\right]^{T} = \left[\frac{1 + \eta_{i}e^{-ik}}{-\sqrt{1 + \eta_{i}^{2} + 2\eta_{i}\cos k}}, 1\right]^{T}, \quad \left[g_{1,k}^{(+)}, g_{2,k}^{(+)}\right]^{T} = \left[\frac{1 + \eta_{i}e^{-ik}}{\sqrt{1 + \eta_{i}^{2} + 2\eta_{i}\cos k}}, 1\right]^{T}, \tag{S5}$$

into

$$\left[h_{1,k}^{(-)}, h_{2,k}^{(-)}\right]^{T} = \left[\frac{1 + \eta_{f}e^{-ik}}{-\sqrt{1 + \eta_{f}^{2} + 2\eta_{f}\cos k}}, 1\right]^{T}, \quad \left[h_{1,k}^{(+)}, h_{2,k}^{(+)}\right]^{T} = \left[\frac{1 + \eta_{f}e^{-ik}}{\sqrt{1 + \eta_{f}^{2} + 2\eta_{f}\cos k}}, 1\right]^{T}. \tag{S6}$$

After the time boundary, the initial state transforms into $|f\rangle$ [Eq. (5)] of the MT, where the creation operator in k-space is $\hat{b}_{\alpha,k}^{\dagger} = \frac{1}{\sqrt{L}} \sum_{l,m} \hat{a}_{l,m}^{\dagger} h_{m,k}^{(\alpha)} e^{ikl}$. The coefficient $\psi_{k,k'}^{(\alpha,\beta)} = \langle \alpha,k;\beta,k'|i\rangle$ with $|\alpha,k;\beta,k'\rangle = \hat{b}_{\alpha,k}^{\dagger} \hat{b}_{\beta,k'}^{\dagger} |0\rangle$. Substituting the creation operators into $\psi_{k,k'}^{(\alpha,\beta)}$, we can get

$$\psi_{k,k'}^{(\alpha,\beta)} = \pm \psi_{k',k}^{(\beta,\alpha)} = \sum_{m_1,m_2} \left[h_{m_2,k'}^{(\beta)*} h_{m_1,k}^{(\alpha)*} \delta_{k_1 k} \delta_{k_2 k'} \pm h_{m_1,k'}^{(\beta)*} h_{m_2,k}^{(\alpha)*} \delta_{k_1 k'} \delta_{k_2 k} \right] g_{m_1,k_1}^{(-)} g_{m_2,k_2}^{(-)}, \tag{S7}$$

where + (-) is for bosonic (fermionic) excitations obeying the operator commutation (anticommutation) relation. Eq. (S7) implies that $\psi_{k\,k'}^{(\alpha,\beta)} \neq 0$ only when $k=k_1$ and $k'=k_2$ or when $k=k_2$ and $k'=k_1$. This is an embody of momentum conservation.

Since identical particle systems do not exhibit operational entanglement, we must label the two particles with specific projective operators [1]. There are two possible ways, that is, \hat{Q}_B and \hat{Q}_M in the MT. For \hat{Q}_B , the post-measurement state is derived

$$|f_{Q}\rangle = \hat{Q}_{B}|f\rangle = \phi_{-,-}|-\rangle_{I}|-\rangle_{II} + \phi_{-,+}|-\rangle_{I}|+\rangle_{II} + \phi_{+,-}|+\rangle_{I}|-\rangle_{II} + \phi_{+,+}|+\rangle_{I}|+\rangle_{II},$$
(S8)

where $\phi_{\alpha,\beta} = \langle \alpha, k_1; \beta, k_2 | f \rangle = 2\psi_{k_1,k_2}^{(\alpha,\beta)}$ for both fermionic and bosonic excitations. The post-measurement density matrix is presented as

$$\hat{\rho}_{B} = |f_{Q}\rangle\langle f_{Q}| = \begin{pmatrix} |\phi_{-,-}|^{2} & \phi_{-,-}\phi_{+,-}^{*} & \phi_{-,-}\phi_{+,-}^{*} & \phi_{-,-}\phi_{+,+}^{*} \\ \phi_{-,+}\phi_{-,-}^{*} & |\phi_{-,+}|^{2} & \phi_{-,+}\phi_{+,-}^{*} & \phi_{-,+}\phi_{-,-}^{*} \\ \phi_{+,-}\phi_{-,-}^{*} & \phi_{+,-}\phi_{-,+}^{*} & |\phi_{+,-}|^{2} & \phi_{+,-}\phi_{-,-}^{*} \\ \phi_{+,+}\phi_{-,-}^{*} & \phi_{+,+}\phi_{+,-}^{*} & |\phi_{+,+}\phi_{-,-}^{*} & |\phi_{+,+}\phi_{-,-}^{*} \end{pmatrix},$$
(S9)

and thus the reduced density matrix for part I is

$$\tilde{\rho}_{\rm B} = \sum_{\beta} {}_{\rm II} \langle \beta | \hat{\rho}_{\rm B} | \beta \rangle_{\rm II} = \begin{pmatrix} |\phi_{-,-}|^2 + |\phi_{-,+}|^2 & \phi_{-,-}\phi_{+,-}^* + \phi_{-,+}\phi_{+,+}^* \\ \phi_{+,-}\phi_{-,-}^* + \phi_{+,+}\phi_{-,+}^* & |\phi_{+,-}|^2 + |\phi_{+,+}|^2 \end{pmatrix}. \tag{S10}$$

Instituting Eq. (S5-S7)) into (S10) results in $S = -\text{Tr}(\tilde{\rho}_B \log_2 \tilde{\rho}_B) \equiv 0$, indicating that the projective measurement by \hat{Q}_B does not induce operational entanglement.

The case is different for \hat{Q}_{M} and the corresponding post-measurement state reads

$$|f_O\rangle = \hat{Q}_{\rm M}|f\rangle = \psi_{k_1,k_2}|k_1\rangle_{\rm I}|k_2\rangle_{\rm II} + \psi_{k_2,k_1}|k_2\rangle_{\rm I}|k_1\rangle_{\rm II},$$
 (S11)

i.e., the Eq. (7) in the MT with $\psi_{k,k'} = \langle -,k;+,k'|f \rangle = 2\psi_{k,k'}^{(-,+)}$. Obviously, $|f_Q\rangle$ demonstrates a momentum entanglement. To let $|f_Q\rangle$ be a Bell state, the condition $|\psi_{k_1k_2}| = |\psi_{k_2k_1}|$ is required. To find the solution of $|\psi_{k_1,k_2}| = |\psi_{k_2,k_1}|$, we perform Taylor expansions for ψ_{k_1,k_2} , ψ_{k_2,k_1} up to the first order of $\Delta k = k_2 - k_1$, resulting in,

$$\psi_{k_1,k_2} \approx \left[2 - 2e^{2i\Xi(k_0)}\right] + 8ie^{i\Xi(k_0)} \mathcal{Z}(k_0, \eta_i, \eta_f) \cdot \Delta k,\tag{S12}$$

$$\psi_{k_2,k_1} \approx (-1)^{q_1} \left[2 - 2e^{2i\Xi(k_0)} \right] + (-1)^{q_2} 8ie^{i\Xi(k_0)} \mathcal{Z}(k_0, \eta_i, \eta_f) \cdot \Delta k, \tag{S13}$$

with

$$\Xi(k_0) \equiv \arctan \frac{\eta_f \sin k_0}{1 + \eta_f \cos k_0} - \arctan \frac{\eta_i \sin k_0}{1 + \eta_i \cos k_0}, \tag{S14}$$

$$\Xi(k_0) \equiv \arctan \frac{\eta_f \sin k_0}{1 + \eta_f \cos k_0} - \arctan \frac{\eta_i \sin k_0}{1 + \eta_i \cos k_0},$$

$$Z(k_0, \eta_i, \eta_f) \equiv \frac{\eta_f \cos k_0 + \eta_f^2}{1 + \eta_f^2 + 2\eta_f \cos k_0} - \frac{\eta_i \cos k_0 + \eta_i^2}{1 + \eta_i^2 + 2\eta_i \cos k_0}$$
(S14)

Note that we have $q_1 = 0$ and $q_2 = 1$ for bosonic excitations, while have $q_1 = 1$ and $q_2 = 0$ for fermionic excitations.

As the terms of the zeroth order of Δk have the same amplitude, we can simply set $\mathcal{Z}(k_0, \eta_i, \eta_f) = 0$ to obtain $\psi_{k_1, k_2} = +\psi_{k_2, k_1}$ for bosonic excitations while $\psi_{k_1,k_2} = -\psi_{k_2,k_1}$ for fermionic ones, up to the first order in $O(\Delta k)$. The condition of $\mathcal{Z}(k_0,\eta_i,\eta_f) = 0$ leads to the parametric equation

$$\cos k_0 = -\frac{\eta_i + \eta_f}{1 + \eta_i \eta_f} \quad (\eta_i \neq \eta_f; \ \eta_i, \eta_f \notin \{0, 1\}), \tag{S16}$$

i.e. the Eq. (8) in the MT. The solution space is plotted in Fig. 2a of the MT. A strict solution can be found, that is, when $k_0 = 0.5\pi$, we can get $\cos k_1 = -\cos k_2$, $\sin k_1 = \sin k_2$ due to $k_1 = k_0 - \Delta k/2$ and $k_2 = k_0 + \Delta k/2$. Under this relationship, $\psi_{k_1,k_2}^{(-,+)} = \pm \psi_{k_2,k_1}^{(-,+)}$ can be derived from Eqs. (S5), (S6) and (S7) when $\eta_i = -\eta_f$, and thus $\psi_{k_1,k_2} \equiv \pm \psi_{k_2,k_1}$ for bosonic and fermionic excitations, respectively. Namely, the solution of $\eta_i = -\eta_f$ and $k_0 = \frac{\pi}{2}$ ensures that $|f_Q\rangle$ is strictly a Bell state.

Appendix III: Time boundary induced by tuning onsite energies

In the preceding discussion, time boundaries were induced by temporally tuning the normalized inter-cell coupling strength η . In this section, we present an alternative scheme where the time boundary is introduced via the tuning of onsite energies [2]. To this end, we modify the Hamiltonian (Eq. (1) of the MT) of the SSH model for M = 2 as follows:

$$\hat{\mathcal{H}} = \sum_{l} \left[v \hat{a}_{l,1}^{\dagger} \hat{a}_{l,2} + w \hat{a}_{l,2}^{\dagger} \hat{a}_{l+1,1} + h.c. \right] + \sum_{l} \Delta(t) \left[\hat{a}_{l,1}^{\dagger} \hat{a}_{l,1} - \hat{a}_{l,2}^{\dagger} \hat{a}_{l,2} \right], \tag{S17}$$

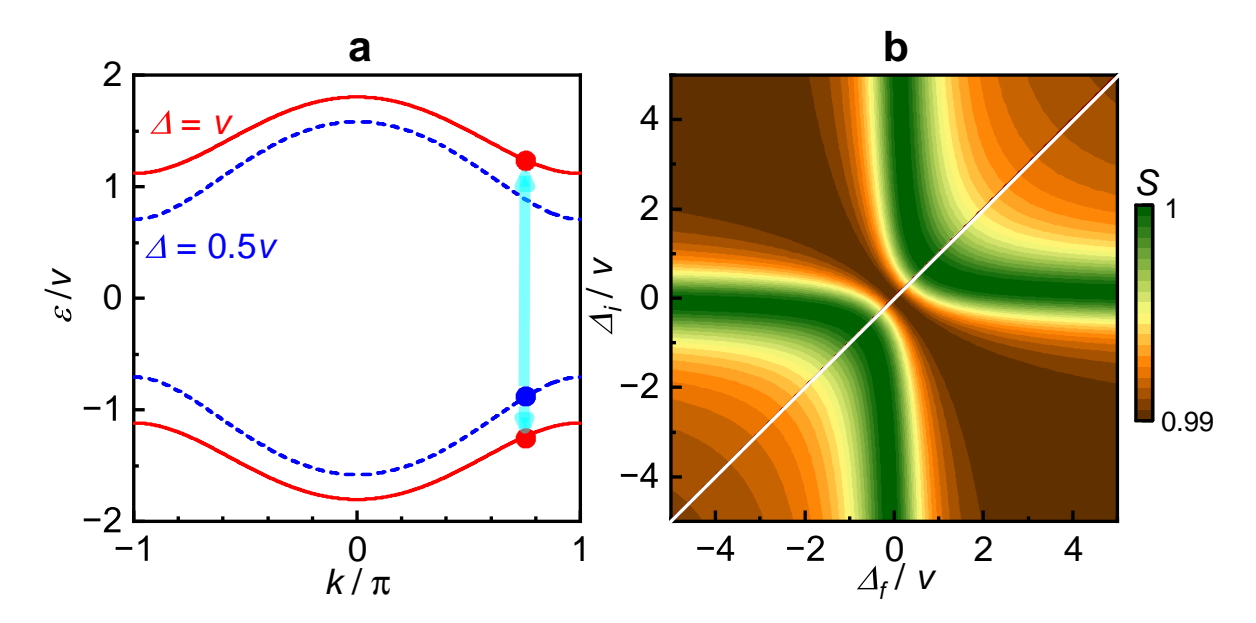


Figure S1. **a**.The band structures of the SSH model (M=2) with $\Delta=0.5v$ (blue dash lines) and $\Delta=v$ (red solid lines). **b**. Variation of von Neumann entropy for $|f_O\rangle$ with Δ_i and Δ_f . Parameters: $k_0=0.75\pi$, $\Delta k=0.02\pi$, and w=0.5v.

where $\pm\Delta(t)$ denote the time-varying onsite energies of the two sites in each unit cell (which are assumed to be zero in the MT), and v, w are constants. According to Eqs. (S1) to (S3), the dispersion relation of this system is derived as $\varepsilon_{\pm}(k, \Delta) = \pm \sqrt{v^2 + w^2 + 2vw\cos k + \Delta^2(t)}$. When the time boundary t_c is encountered, the absolute value of the onsite energy transitions from Δ_i to Δ_f , inducing a transformation of the system's eigenstates from

$$\left[g_{1,k}^{(-)}, g_{2,k}^{(-)}\right]^{T} = \left[\frac{v + we^{-ik}}{\varepsilon_{-}(k, \Delta_{i}) - \Delta_{i}}, 1\right]^{T}, \quad \left[g_{1,k}^{(+)}, g_{2,k}^{(+)}\right]^{T} = \left[\frac{v + we^{-ik}}{\varepsilon_{+}(k, \Delta_{i}) - \Delta_{i}}, 1\right]^{T}$$
(S18)

to

$$\left[h_{1,k}^{(-)}, h_{2,k}^{(-)}\right]^{T} = \left[\frac{v + we^{-ik}}{\varepsilon_{-}(k, \Delta_{f}) - \Delta_{f}}, 1\right]^{T}, \quad \left[h_{1,k}^{(+)}, h_{2,k}^{(+)}\right]^{T} = \left[\frac{v + we^{-ik}}{\varepsilon_{+}(k, \Delta_{f}) - \Delta_{f}}, 1\right]^{T}. \tag{S19}$$

Under this time scattering mechanism, the energy bands for $\Delta = 0.5v$ and $\Delta = v$ are presented in Fig. S1a. Momentum conservation is preserved throughout the time scattering process. When Δ transitions from $\Delta_i = 0.5v$ into $\Delta_f = v$, the initial state constructed around the blue dot in Fig. S1a would redistributes into states around the two red dots.

The procedure for exploring the entanglement induced by this time scattering process follows the same framework as that described in Sec. II. Though it is difficult to derive the elegant analytical solution like Eq. (S16) (or Eq. (8) of the MT) in this case, we can still demonstrate the potential to construct Bell states via numerical simulation. Starting from the initial state defined in Eq. (4) of the MT, we derive the post-measurement state [Eq. (S11), corresponding to Eq. (7) of the MT] through time-boundary scattering and projective measurement. The key modified here is to substitute Eqs. (S18) and (S19) into Eq. (S7). Figure S1b presents the von Neumann entropies $S = -|\psi_{k_1,k_2}|^2 \log_2|\psi_{k_1,k_2}|^2 - |\psi_{k_2,k_1}|^2 \log_2|\psi_{k_2,k_1}|^2$ in the Δ_i - Δ_f space with $k_1 = 0.74\pi$, $k_2 = 0.76\pi$, where $\Delta_i \neq \Delta_f$ is necessary for inducing time boundary. These results demonstrate that Bell states (characterized by $S \to 1$) can also be readily obtained via time scattering mechanism.

Appendix IV: Proof of the robustness of Bell states against gradual time boundary

In the MT, we have numerically confirmed that gradual time boundaries do not disrupt the constructed Bell states. To theoretically interpret this phenomenon, we explore this issue by comparing two types of time scattering processes. The first type involves the normalized inter-cell coupling strength sharply transforming from η_i to η_f at time t_c . The time evolution of the system in this process can be vividly represented as

$$|i\rangle \xrightarrow{\eta_i \to \eta_f} |f\rangle.$$
 (S20)

For the other type, the normalized inter-cell coupling strength firstly transforms from η_i to η_p at time t_p and then to η_f at time t_c , i.e.,

$$|i\rangle \frac{\eta_i \to \eta_p}{\text{at } t_p} |p\rangle \frac{\eta_p \to \eta_f}{\text{at } t_c} |f\rangle.$$
 (S21)

First type

For this type, the initial state $|i\rangle$ (Eq. (4) of MT) is straightly transformed into $|f\rangle = \sum_{\alpha\beta,kk'} \psi_{k,k'}^{(\alpha,\beta)} \hat{b}_{\beta,k}^{\dagger} |0\rangle$ at time t_c with

$$\psi_{k\,k'}^{(\alpha,\beta)} = e^{-i\varepsilon_i t_c} \langle 0|\hat{b}_{\beta,k'} \hat{b}_{\alpha,k} | i \rangle = e^{-i\varepsilon_i t_c} {}_f \langle \alpha, k; \beta, k' | i \rangle, \tag{S22}$$

where ε_i is the energy of $|i\rangle$. According to the description in Sec. II, under the condition $\psi_{k_1,k_2}^{(-,+)} = \pm \psi_{k_2,k_1}^{(-,+)}$, i.e.,

$$f\langle -, k_1; +, k_2 | i \rangle = \pm_f \langle -, k_2; +, k_1 | i \rangle, \tag{S23}$$

the Bell states can be constructed.

Second type

In this process, the initial state $|i\rangle$ is transformed into an intermediate state with the form as $|p\rangle = \sum_{\mu\nu,\bar{k}\bar{k}'} \phi_{\bar{k},\bar{k}'}^{(\mu,\nu)} \hat{c}_{\mu,\bar{k}}^{\dagger} \hat{c}_{\nu,\bar{k}'}^{\dagger} |0\rangle$ firstly and then transformed into $|f\rangle$. The coefficient $\phi_{\bar{k}}^{(\mu,\nu)}$ has form

$$\phi_{\tilde{t}\tilde{t}'}^{(\mu,\nu)} = e^{-i\varepsilon_i t_p} \langle 0|\hat{c}_{\nu,\tilde{k}'}\hat{c}_{\mu,\tilde{k}}|i\rangle = e^{-i\varepsilon_i t_p} {}_p \langle \mu,\tilde{k};\nu,\tilde{k}'|i\rangle. \tag{S24}$$

Accordingly, the coefficient $\psi_{k\,k'}^{(\alpha\beta)}$ for $|f\rangle$ is derived as

$$\psi_{k,k'}^{(\alpha,\beta)} = {}_{f}\langle \alpha, k; \beta, k' | \sum_{\mu\nu, \tilde{k}\tilde{k}'} e^{-i\varepsilon_{p}^{(\mu\tilde{k},\nu\tilde{k}')}(t_{c}-t_{p})} \phi_{\tilde{k},\tilde{k}'}^{(\mu,\nu)} \hat{c}_{\mu,\tilde{k}}^{\dagger} \hat{c}_{\nu,\tilde{k}'}^{\dagger} | 0 \rangle, \tag{S25}$$

where $\varepsilon_p^{(\mu \tilde{k}, \nu \tilde{k}')}$ is the energy of the state $|\mu, \tilde{k}; \nu, \tilde{k}'\rangle_p$. Instituting Eq. (S24) into (S25), we can get

$$\psi_{k,k'}^{(\alpha,\beta)} = \sum_{\mu\nu,\tilde{k}\tilde{k}'} e^{-i\varepsilon_{i}t_{p}} e^{-i\varepsilon_{p}^{(\mu\tilde{k},\nu\tilde{k}')}(t_{c}-t_{p})} {}_{f}\langle\alpha,k;\beta,k'|\mu,\tilde{k};\nu,\tilde{k}'\rangle_{pp}\langle\mu,\tilde{k};\nu,\tilde{k}'|i\rangle}$$

$$= e^{-i\varepsilon_{i}t_{p}} {}_{f}\langle\alpha,k;\beta,k'|i\rangle \sum_{\mu\nu,\tilde{k}\tilde{k}'} e^{-i\varepsilon_{p}^{(\mu\tilde{k},\nu\tilde{k}')}(t_{c}-t_{p})} {}_{p}\langle\mu,\tilde{k};\nu,\tilde{k}'|i\rangle|^{2}}$$
(S26)

If Eq. (S23) is satisfied, we can also obtain the necessary and sufficient condition for constructing Bell states from Eq. (S26), i.e., $\psi_{k_1,k_2}^{(-,+)} = \pm \psi_{k_2,k_1}^{(-,+)}$. By comparing the two types of time scattering processes, we conclude that as long as the parametric conditions for Bell states

By comparing the two types of time scattering processes, we conclude that as long as the parametric conditions for Bell states in Eq. (S16) (i.e., Eq. (8) in the MT) are satisfied, the intermediate time boundary does not affect the construction of Bell states. This conclusion can also be extended to scenarios with more intermediate time boundaries in the time scattering process, which is responsible for the robustness of the Bell states against gradual time boundaries.

Appendix V: Proof of the robustness of Bell states against environmental decoherence

To theoretically interpret the robustness of the constructed Bell states against environmental decoherence and ensure the post-projected state is a pure state, the Lindblad master equation in *k*-space is employed:

$$\frac{d\hat{\rho}}{dt} = -i\left[\hat{\mathcal{H}}, \, \hat{\rho}\right] + \gamma \sum_{\alpha,k} \left(\hat{a}_{\alpha,k} \hat{\rho} \hat{a}_{\alpha,k}^{\dagger} - \frac{1}{2} \left\{\hat{\rho}, \hat{a}_{\alpha,k}^{\dagger} \hat{a}_{\alpha,k}\right\}\right),\tag{S27}$$

with the initial state taken as Eq. (4) in the MT. The Hamiltonian $\hat{\mathcal{H}}$ as Eq. (1) of the MT is rewritten into

$$\hat{\mathcal{H}} = \sum_{\alpha,k} \varepsilon_{\alpha}(k) \hat{a}_{\alpha,k}^{\dagger} \hat{a}_{\alpha,k} |0\rangle \tag{S28}$$

through Fourier transformation. Notably, the Hamiltonian (S28) represents its form before the time boundary. To derive its form after the time boundary, we need to substitute the $\hat{a}^{\dagger}_{\alpha,k}$ ($\hat{a}_{\alpha,k}$) by $\hat{b}^{\dagger}_{\alpha,k}$ ($\hat{b}_{\alpha,k}$). Under the state bases $|n\rangle_i$ (before time boundary), defined as,

$$|1\rangle_{i} = |0\rangle, |2\rangle_{i} = |-, k_{1}\rangle_{i}, |3\rangle_{i} = |-, k_{2}\rangle_{i}, |4\rangle_{i} = |+, k_{1}\rangle_{i}, |5\rangle_{i} = |+, k_{2}\rangle_{i}, |6\rangle_{i} = |-, k_{1}; -, k_{2}\rangle_{i}, |7\rangle_{i} = |-, k_{1}; +, k_{2}\rangle_{i}, |8\rangle_{i} = |+, k_{1}; -, k_{2}\rangle_{i}, |9\rangle_{i} = |+, k_{1}; +, k_{2}\rangle_{i},$$
(S29)

the initial density matrix $\hat{\rho}_i = |i\rangle\langle i|$ has the form,

$$\hat{\rho}_i = \text{diag}(0, 0, 0, 0, 0, 1, 0, 0, 0). \tag{S30}$$

The function

$$\hat{\rho}(t + \Delta t) = \hat{\rho}(t) + \hat{R}(t) \cdot \Delta t \tag{S31}$$

with $\hat{R}(t) = d\hat{\rho}(t)/dt$ dictates the evolution of the density matrix $\hat{\rho}$ from the initial one $\hat{\rho}_i$. It is straightforward to derive that before the time boundary, only four elements of $\hat{\rho}$: $\rho_{1,1}$, $\rho_{2,2}$, $\rho_{3,3}$ and $\rho_{6,6}$ evolve into nonzero terms, whereas all other elements remain at their initial values. Accordingly, we write $\hat{\rho}(t_c^-)$ at the time infinitesimally close to t_c as

$$\hat{\rho}(t_c^-) = \operatorname{diag}(\rho_{11}^{(c^-)}, \rho_{22}^{(c^-)}, \rho_{33}^{(c^-)}, 0, 0, \rho_{66}^{(c^-)}, 0, 0, 0). \tag{S32}$$

When the time boundary is encountered, the state bases turns into $|n\rangle_f$, defined as,

$$\begin{split} |1\rangle_f &= |0\rangle, & |2\rangle_f &= |-, k_1\rangle_f, & |3\rangle_f &= |-, k_2\rangle_f, \\ |4\rangle_f &= |+, k_1\rangle_f, & |5\rangle_f &= |+, k_2\rangle_f, & |6\rangle_f &= |-, k_1; -, k_2\rangle_f, \\ |7\rangle_f &= |-, k_1; +, k_2\rangle_f, & |8\rangle_f &= |+, k_1; -, k_2\rangle_f, & |9\rangle_f &= |+, k_1; +, k_2\rangle_f. \end{split} \tag{S33}$$

The two state bases have the following transformative relations, i.e.,

$$|1\rangle_f = |1\rangle_i,\tag{S34}$$

$$|2\rangle_f = a_1|2\rangle_i + a_2|4\rangle_i,\tag{S35}$$

$$|3\rangle_f = b_1|3\rangle_i + b_2|5\rangle_i,\tag{S36}$$

$$|4\rangle_f = c_1|2\rangle_i + c_2|4\rangle_i,\tag{S37}$$

$$|5\rangle_f = d_1|3\rangle_i + d_2|5\rangle_i,\tag{S38}$$

$$|6\rangle_f = a_1b_1|6\rangle_i + a_1b_2|7\rangle_i + a_2b_1|8\rangle_i + a_2b_2|9\rangle_i,$$
(S39)

$$|7\rangle_f = a_1 d_1 |6\rangle_i + a_1 d_2 |7\rangle_i + a_2 d_1 |8\rangle_i + a_2 d_2 |9\rangle_i, \tag{S40}$$

$$|8\rangle_f = b_1 c_1 |6\rangle_i + b_2 c_1 |7\rangle_i + b_1 c_2 |8\rangle_i + b_2 c_2 |9\rangle_i,$$
(S41)

$$|9\rangle_f = c_1 d_1 |6\rangle_i + c_1 d_2 |7\rangle_i + c_2 d_1 |8\rangle_i + c_2 d_2 |9\rangle_i,$$
(S42)

where a, b, c, and d denote the non-zero transformative coefficients. These transformative relations are responsible for the following form of the density operator at the time infinitesimally after t_c ,

$$\hat{\rho}(t_c^+) = \begin{pmatrix} \rho_{1,1}^{(c^+)} & 0 & 0 & 0 & 0 & 0 & 0 & 0 & 0 \\ 0 & \rho_{2,2}^{(c^+)} & 0 & \rho_{2,4}^{(c^+)} & 0 & 0 & 0 & 0 & 0 \\ 0 & 0 & \rho_{3,3}^{(c^+)} & 0 & \rho_{3,5}^{(c^+)} & 0 & 0 & 0 & 0 \\ 0 & \rho_{4,2}^{(c^+)} & 0 & \rho_{4,4}^{(c^+)} & 0 & 0 & 0 & 0 & 0 \\ 0 & 0 & \rho_{5,3}^{(c^+)} & 0 & \rho_{5,5}^{(c^+)} & 0 & 0 & 0 & 0 \\ 0 & 0 & 0 & 0 & 0 & \rho_{5,6}^{(c^+)} & \rho_{6,7}^{(c^+)} & \rho_{6,8}^{(c^+)} & \rho_{6,9}^{(c^+)} \\ 0 & 0 & 0 & 0 & 0 & \rho_{7,6}^{(c^+)} & \rho_{7,7}^{(c^+)} & \rho_{7,8}^{(c^+)} & \rho_{7,9}^{(c^+)} \\ 0 & 0 & 0 & 0 & 0 & \rho_{8,6}^{(c^+)} & \rho_{8,7}^{(c^+)} & \rho_{8,8}^{(c^+)} & \rho_{8,9}^{(c^+)} \\ 0 & 0 & 0 & 0 & 0 & \rho_{9,6}^{(c^+)} & \rho_{9,7}^{(c^+)} & \rho_{9,8}^{(c^+)} & \rho_{9,9}^{(c^+)} \end{pmatrix},$$
(S43)

where the zero and nonzero elements are explicitly denoted. The density matrix $\hat{\rho}_f$ at time t (larger than t_c) is determined by Eqs. (S31) and (S43). Since the $\hat{\rho}_M = \hat{Q}_M \hat{\rho}_f \hat{Q}_M^{\dagger}$ only involves the state bases $|7\rangle_f$ and $|8\rangle_f$, we just need to attend the matrix

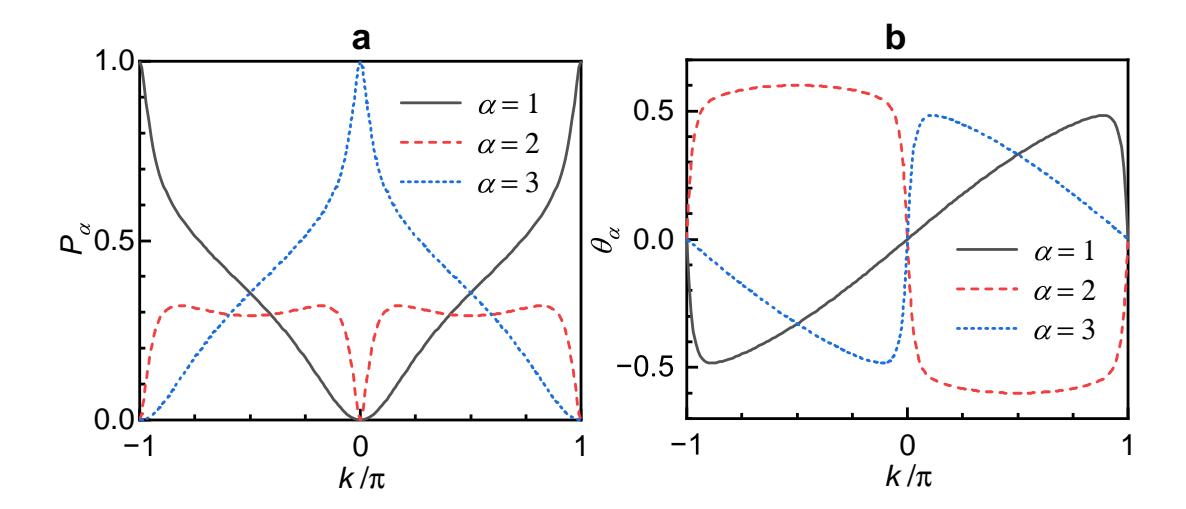


Figure S2. **a.** Variations of scattering probabilities to B1, B2 and B3 bands from B*i*. **b.** Variations of scattering angles θ for B1, B2 and B3 bands. Parameters: $k_0 = 0.75\pi$, $\eta_i = 0.5$ and $\eta_f = -1.1$.

elements $R_{p,q}(t)$ with $p, q \in \{7, 8\}$ for $\hat{R}(t)$ in Eq. (S31). According to the Lindblad master equation Eq. (S27), these elements have the form,

$$R_{p,q}(t) = -2\gamma \rho_{p,q}(t), \tag{S44}$$

and thus

$$\hat{\rho}_{M}(t + \Delta t) = (1 - 2\gamma \Delta t) \begin{pmatrix} \rho_{7,7}(t) & \rho_{7,8}(t) \\ \rho_{8,7}(t) & \rho_{8,8}(t) \end{pmatrix} = (1 - 2\gamma \Delta t)\hat{\rho}_{M}(t).$$
 (S45)

This leads to $\hat{\rho}_{\rm M}(t) = \hat{\rho}_{\rm M}(t_c^+)e^{-2\gamma(t-t_c^+)}$ and subsequently, the entanglement of $\hat{\rho}_{\rm M}(t)$ is identical to that of $\hat{\rho}_{\rm M}(t_c^+)$. Moreover, by leveraging Eq. (S43), we derive the normalized $\hat{\rho}_{\rm M}(t_c^+)$ as,

$$\hat{\rho}_{\mathbf{M}}(t_c^+) = \begin{pmatrix} \rho_{7,7}^{(c^+)} & \rho_{7,8}^{(c^+)} \\ \rho_{8,7}^{(c^+)} & \rho_{8,8}^{(c^+)} \end{pmatrix} = \frac{1}{|a_1d_1|^2 + |b_1c_1|^2} \begin{pmatrix} |a_1d_1|^2 & a_1^*d_1^*b_1c_1 \\ a_1d_1b_1^*c_1^* & |b_1c_1|^2 \end{pmatrix}. \tag{S46}$$

It is easy to verify $\text{Tr}\left[\hat{\rho}_{\text{M}}^{2}(t_{c}^{+})\right]=1$ and thus the post-projected operator $\hat{\rho}_{\text{M}}(t)$ describes a pure state. Under the condition of Eq. (S16), $\hat{\rho}_{\text{M}}(t)$ corresponds to a momentum-entangled Bell state. The above proof confirms the phenomenon described in the MT: the constructed Bell states exhibit robustness against environmental decoherence.

Appendix VI: Multifold time scattering and highly entangled states

In the MT, it is stated that the systems with M > 2 can induce multifold time scattering, and the case of M = 3 is illustrated in Fig. 4. The scattering particles on different bands separate spatially due to their distinct group velocities. According to the description in Sec. I, the group velocities of $B\alpha$ band is $v_{\alpha} = d\varepsilon_{\alpha}(k)/dk$, and the scattering probability from Bi to $B\alpha$ band is quantified by $P_{\alpha} = |\mathbf{u}_{\alpha}^{*}(k) \cdot \mathbf{u}_{i}(k)|^{2}$. Taking M = 3 as an example, the scattering probabilities of all bands, varying with wave vector k, are presented in Fig. S2a. The incident angle θ_{i} and scattering angles θ_{α} , marked in Fig. 4b of the MT, are relevant to the group velocities of each band. These angles are defined in a renormalized "space-time" plane since space and time have different units. We here take the lattices constant and reciprocal of intra-cell coupling (v^{-1}) to renormalize space and time, respectively [3], and subsequently obtain

$$\tan \theta_i = v_i/v, \quad \tan \theta_\alpha = v_\alpha/v, \quad \alpha \in \{1, 2, \cdots M\}. \tag{S47}$$

For the case of M=3, the variations of the scattering angles with k are plotted in Fig. S2b. If taking the parameters in Fig. 4b, i.e., $\eta_i=0.5$, $\eta_f=-1.1$, and $k_0=0.75\pi$, one has the three angles as $\theta_1=25.7^\circ$, $\theta_2=-33.4^\circ$, and $\theta_3=10.1^\circ$, where the minus sign represents the reflection.

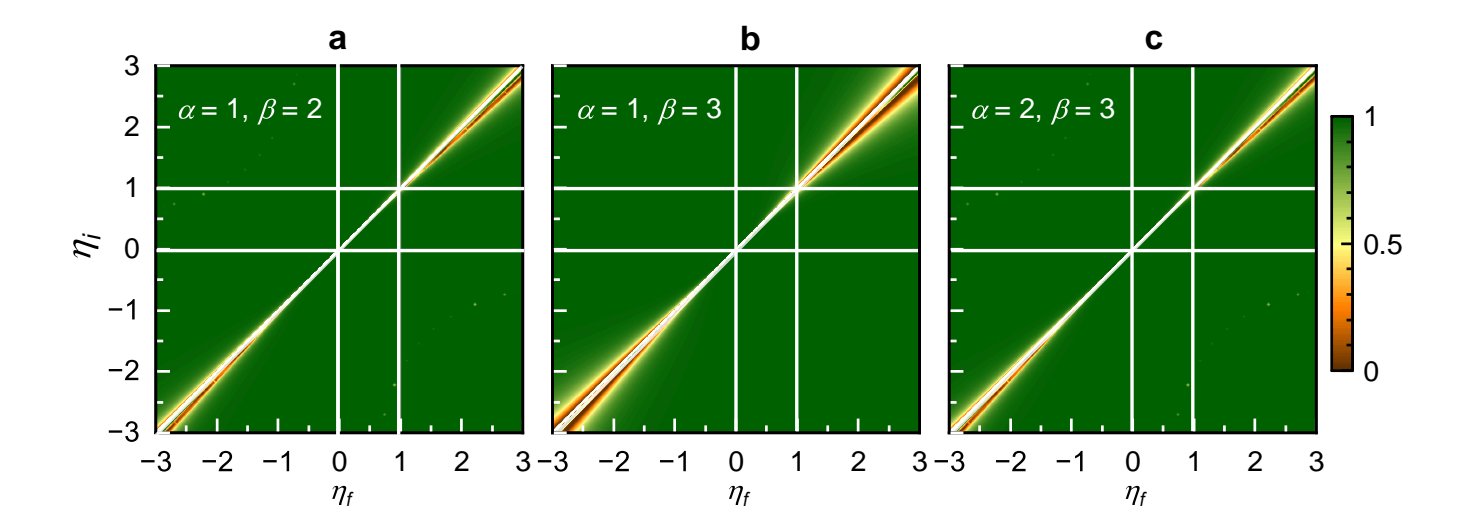


Figure S3. Variations of von Neumann entropies for $|f_O^{(\alpha,\beta)}\rangle$ with η_i and η_f . Parameters: $k_0 = 0.75\pi$, $\Delta k = 0.02\pi$.

Figure 4c of the MT has confirmed the presence of high-momentum entanglements in multi-band systems under specific parameter values. For the case of M = 3, the parametric conditions for preparing these highly entangled states can be numerically explored. Similar to the M = 2 case, we start from the initial state

$$|i\rangle = \hat{a}_{ik_1}^{\dagger} \hat{a}_{ik_2}^{\dagger} |0\rangle, \tag{S48}$$

which represents a two-particle plane-wave pulse constructed on the Bi band (see Fig. 4a in the MT), with $k_1 \neq k_2$ assumed. This state finally evolves into

$$|f\rangle = \sum_{\mu\nu,kk'} \psi_{k,k'}^{(\mu,\nu)} \hat{b}_{\mu,k}^{\dagger} \hat{b}_{\nu,k'}^{\dagger} |0\rangle \tag{S49}$$

where $\mu, \nu \in \{1, 2, ..., M\}$. Through projection with the operator $\hat{Q}_{M}^{(\alpha, \beta)}$, the post-projected state is derived as

$$|f_Q^{(\alpha,\beta)}\rangle = \hat{Q}_{\rm M}^{(\alpha,\beta)}|f\rangle = \phi_{k_1,k_2}^{(\alpha,\beta)}|k_1\rangle_{\rm II} + \phi_{k_2,k_1}^{(\alpha,\beta)}|k_2\rangle_{\rm I}|k_1\rangle_{\rm II}, \tag{S50}$$

where $|k\rangle_{\rm I} = |\alpha,k\rangle$, $|k'\rangle_{\rm II} = |\beta,k'\rangle$, and $\phi_{k,k'}^{(\alpha,\beta)} = 2\psi_{k,k'}^{(\alpha,\beta)}$. The form of $\psi_{k,k'}^{(\alpha,\beta)}$ is analogous to that in Eq. (S7), provided that the parameters g and h are adapted to the M-band system. For M=3, the entanglements $S_{\alpha\beta} = -\left|\phi_{k_1,k_2}^{(\alpha,\beta)}\right|^2\log_2\left|\phi_{k_2,k_1}^{(\alpha,\beta)}\right|^2 - \left|\phi_{k_2,k_1}^{(\alpha,\beta)}\right|^2\log_2\left|\phi_{k_2,k_1}^{(\alpha,\beta)}\right|^2$ are illustrated in Fig. S3. The three panels reveal a broad parametric range that induces high entanglements between each pair of bands. Notably, $\eta_i \neq \eta_f$ and $\eta_i, \eta_f \notin \{0,1\}$.

^[1] R. Lo Franco and G. Compagno, Indistinguishability of elementary systems as a resource for quantum information processing, Phys. Rev. Lett. 120, 240403 (2018).

^[2] M. Atala, M. Aidelsburger, J. T. Barreiro, D. Abanin, T. Kitagawa, E. Demler, and I. Bloch, Direct measurement of the zak phase in topological bloch bands, Nature Phys. 9, 795 (2013).

^[3] Z. Dong, H. Li, T. Wan, Q. Liang, Z. Yang, and B. Yan, Quantum time reflection and refraction of ultracold atoms, Nat. Photon. 18, 68 (2024).